CGMS

CGMS-43 JMA-WP-09
Prepared by JMA
Agenda Item: Plenary F.1.7 and II/3
Discussed in Plenary and WG II

# First results and products from Himawari-8

The next-generation geostationary meteorological satellite of the Japan Meteorological Agency (JMA), Himawari-8, was successfully launched on 7 October 2014 and will start operation in July 2015. Himawari-8 features the new 16-band Advanced Himawari Imager (AHI), whose spatial resolution and observation frequency are improved over those of its predecessor MTSAT-series satellites. These improvements will bring unprecedented levels of performance in nowcasting services and short-range weather forecasting systems. In view of the essential nature of navigation and radiometric calibration in fully leveraging the imager's potential, this working paper reports on the current status of navigation and calibration for the AHI and outlines related products.

**Recommendations:** none

# 1 INTRODUCTION

The next-generation geostationary meteorological satellite of the Japan Meteorological Agency (JMA), Himawari-8, was successfully launched on 7 October 2014. The satellite will start operation in July 2015 after the completion of overall-system checking. Himawari-8 features the new Advanced Himawari Imager, which has twice the spatial resolution of its predecessor MTSAT-series satellites. The hardware configuration of the AHI is similar to that of the Advanced Baseline Imager (ABI) on board on the GOES-R satellite. Table 1-1 shows general information on the AHI, the ABI and the IMAGER on board MTSAT-2.

The AHI produces full-disk imagery every 10 minutes, and rapid scanning at 2.5-minute intervals is also conducted. Landmark observation is performed to improve the accuracy of satellite attitude information. The observation function is also utilized for lunar observation. Figure 1-1 shows the observation time line for each 10-minute period. The significant improvements made to the imager will bring unprecedented levels of performance in nowcasting services and short-range weather forecasting systems. In view of the essential nature of navigation and radiometric calibration in fully leveraging the imager's potential, this working paper reports on the current status of navigation and calibration for the AHI and outlines related level-1 and -2 products.

| | Himawari-8/9 | GOES-R | MTSAT-2 |
|---|---|---|---|
| Radiometer | AHI | ABI | IMAGER |
| Bands | 16<br>VIS:3, NIR:3, IR:10 | 16<br>VIS:2, NIR:4, IR:10 | 5<br>VIS:1, IR:4 |
| Spatial resolution (at SSP) | 0.5km, 1km, 2km | 0.5km, 1km, 2km | 1km, 4km |
| Full disk observation plan | Full disk observation is planned every 10 minutes. | Full disk observation is planned every 15 minutes. | Full disk observation is performed hourly. |
| Scan pattern | West to East<br>23 scans cover full disk. | West to East<br>22 scans cover full disk. | Both direction from West and East. Around 1400 scans cover full disk. |
| Orbit determination | Ranging | Ranging + GPS | Ranging |
| Attitude determination | Star tracker + Rate sensor and so forth | Star tracker + Rate sensor and so forth | Sun sensor + Earth sensor |
| Navigation correction | Landmark analysis | Star sensing | Landmark analysis |

Table 1-1 General information on the AHI, the ABI and the IMAGER on board MTSAT-2

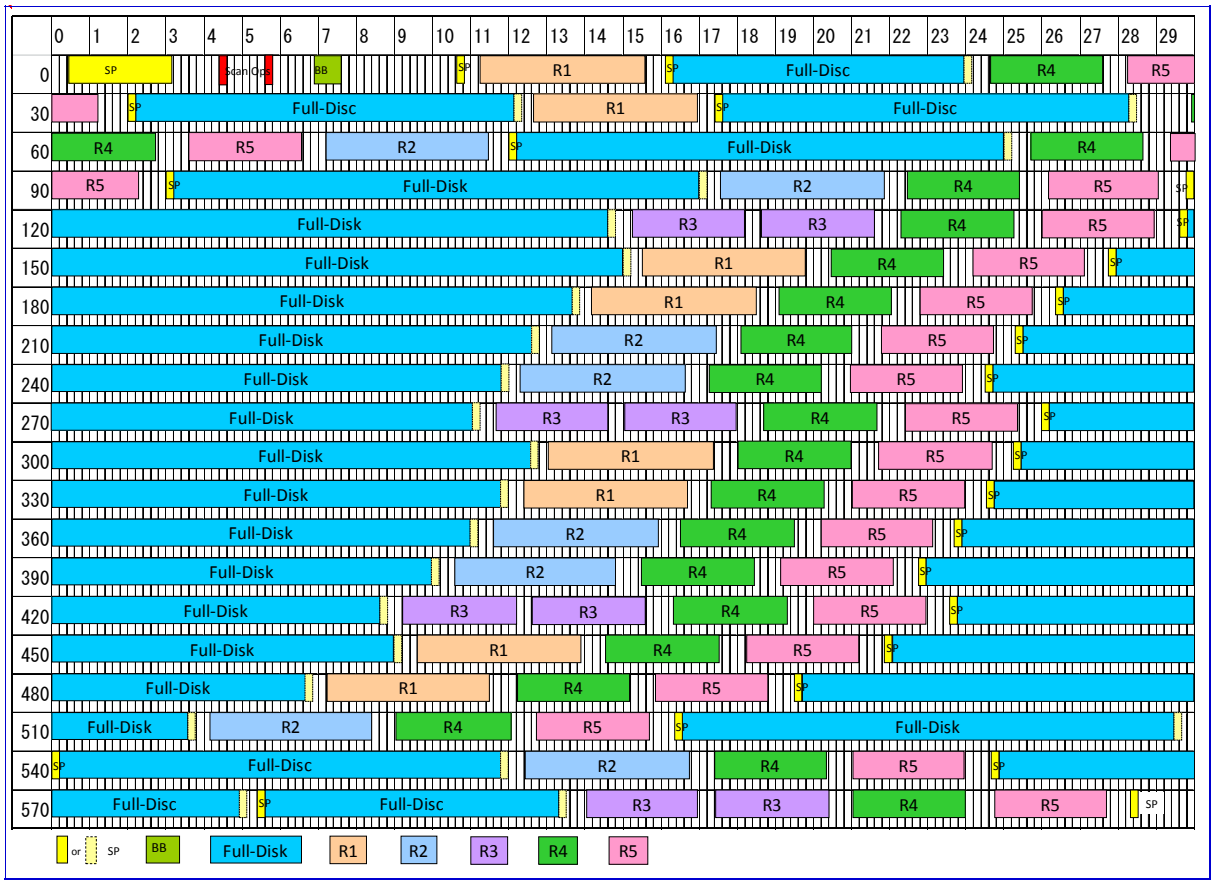


Figure 1-1 AHI observation timeline for each 10-minute period. The green rectangles ("BB") represent black body observation. Deep space observation (shown with yellow rectangles, "SP") is performed at the beginning or end of each swath for full-disk observation (blue rectangles, "Full Disk").

# 2 AHI FACT SHEET

## 2.1 AHI basics

Figure 2-1 and Table 2-1 summarize the observation bands of the AHI on board Himawari-8 and its spectral response functions (SRFs). The AHI is provided by the same vendor as the ABI. The AHI has 0.51 µm bands as opposed to the ABI's 1.38 µm bands. The AHI's composition of three visible bands (blue: 0.47 µm; green: 0.51 µm; red: 0.64 µm) enables the production of true-color images. SRF information is provided on the website[1] of JMA's Meteorological Satellite Center (MSC).

[1] http://www.data.jma.go.jp/mscweb/en/himawari89/space_segment/spsg_ahi.html

| Band | Himawari-8/9 | | MTSAT-2 | |
|---|---|---|---|---|
| | Wave length | Spatial resolution | Wave length | Spatial resolution |
| 1 | 0.47 μm | 1km | | |
| 2 | 0.51 μm | 1km | | |
| 3 | 0.64 μm | 0.5km | 0.68 μm | 1km |
| 4 | 0.86 μm | 1km | | |
| 5 | 1.6 μm | 2km | | |
| 6 | 2.3 μm | 2km | | |
| 7 | 3.9 μm | 2km | 3.7 μm | 4km |
| 8 | 6.2 μm | 2km | 6.8 μm | 4km |
| 9 | 6.9 μm | 2km | | |
| 10 | 7.3 μm | 2km | | |
| 11 | 8.6 μm | 2km | | |
| 12 | 9.6 μm | 2km | | |
| 13 | 10.4 μm | 2km | 10.8 μm | 4km |
| 14 | 11.2 μm | 2km | | |
| 15 | 12.4 μm | 2km | 12.0 μm | 4km |
| 16 | 13.3 μm | 2km | | |

Table 2-1 Basic information on the AHI on board Himawari-8 and the IMAGER on board MTSAT-2

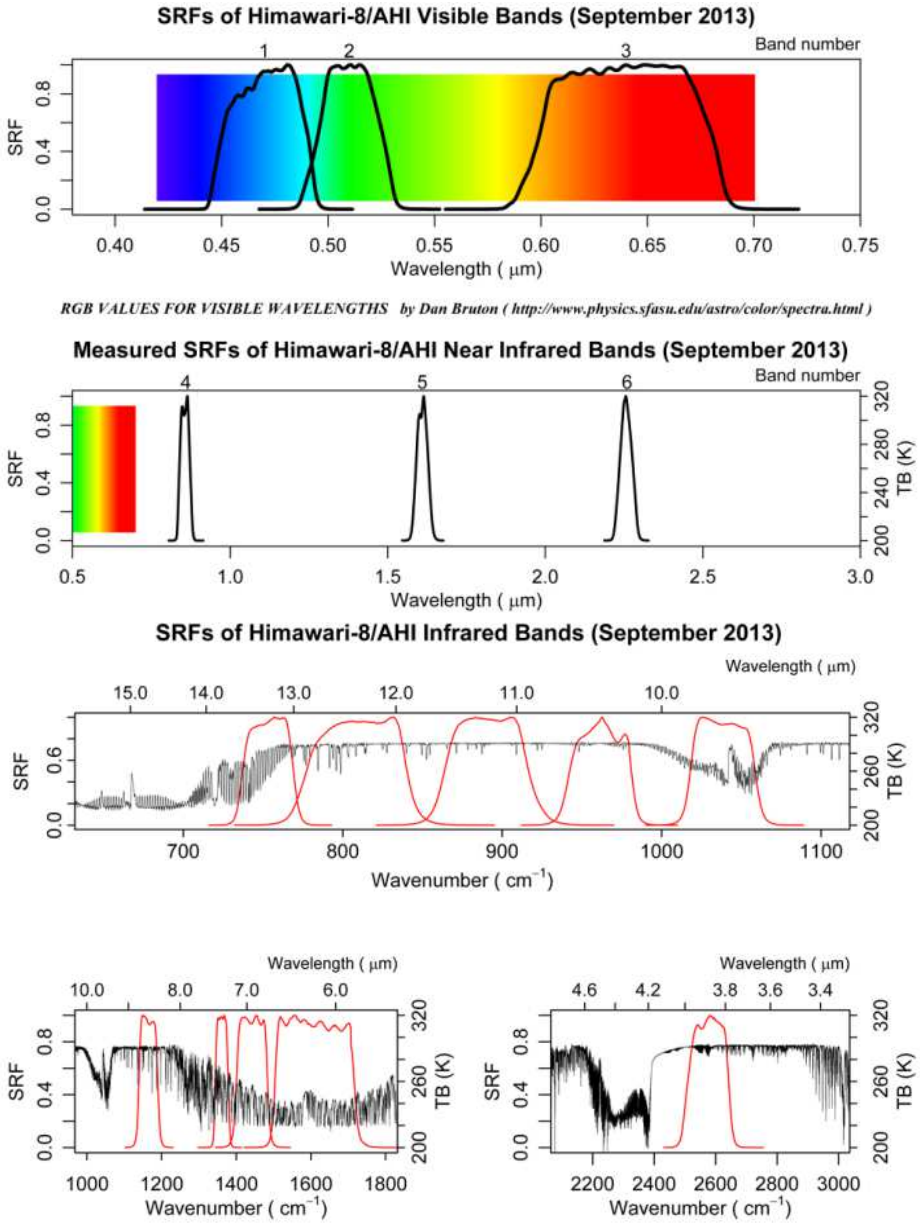


Figure 2-1 AHI spectral response functions

## 2.2 Ground test summary

AHI performance has been evaluated in ground testing. Table 2-2 shows the results, including data on the center wavelength, bandwidth, bit depth, radiometric calibration accuracy, internal calibration target (ICT) emissivity and out-of-band response.

| Band | Center wavelength [μm] | Bandwidth [μm] | Bits | Radiometric calibration accuracy | ICT emissivity (Analysis) | Out-of-band wavelength response |
|---|---|---|---|---|---|---|
| 1 | 0.4703 | 0.0407 | 11 | 2.63% | - | 0.13% |
| 2 | 0.5105 | 0.0308 | 11 | 2.53% | - | 0.36% |
| 3 | 0.6399 | 0.0817 | 11 | 2.55% | - | 0.08% |
| 4 | 0.8563 | 0.0345 | 11 | 2.39% | - | 0.24% |
| 5 | 1.6098 | 0.0409 | 11 | 2.73% | - | 0.31% |
| 6 | 2.257 | 0.0441 | 11 | 2.82% | - | 0.29% |
| 7 | 3.8848 | 0.2006 | 14 | 0.42% | 99.83% | 0.23% |
| 8 | 6.2383 | 0.8219 | 11 | 0.34% | 99.93% | 0.29% |
| 9 | 6.9395 | 0.4019 | 11 | 0.29% | 99.90% | 0.43% |
| 10 | 7.3471 | 0.1871 | 12 | 0.24% | 99.93% | 0.49% |
| 11 | 8.5905 | 0.3727 | 12 | 0.20% | 99.91% | 0.34% |
| 12 | 9.6347 | 0.3779 | 12 | 0.21% | 99.92% | 0.27% |
| 13 | 10.4029 | 0.4189 | 12 | 0.23% | 99.98% | 0.36% |
| 14 | 11.2432 | 0.6678 | 12 | 0.22% | 99.98% | 0.30% |
| 15 | 12.3828 | 0.9656 | 12 | 0.20% | 99.95% | 0.32% |
| 16 | 13.2844 | 0.5638 | 11 | 0.22% | 99.94% | 0.29% |

Table 2-2 Brief summary of AHI performance as evaluated in ground testing. In this table, bandwidth is defined as full width at half maximum. The center wavelength is that of the bandwidth. Radiometric calibration accuracy for bands 1 – 6 show uncertainties from influences including instrumentation and test sources. Accuracy data for bands 7 – 16 are those for ICT radiance. Out-of-band wavelength response is defined as the scene-weighted integral of the relative wavelength response excluding the range between the 1% points. The standard scene is a 100% albedo for bands 1 – 6 and a 300K blackbody for bands 7 – 16.

## 2.3 In-orbit test summary

The optical parameters of the AHI, including IFOV size, EW sampling distance, signal-to-noise ratio (SNR) and dynamic range, were evaluated by the vendor as part of in-orbit testing (IOT). The results showed that all parameters met the specifications. The Appendix gives a summary of IOT for the operational system.

# 3 NAVIGATION

Navigation is based on information from star trackers, inertia reference units and angular rate sensors on board Himawari-8. Navigation and co-registration accuracy is validated using landmark analysis.

## 3.1 AHI navigation basics

Determination of Himawari-8's orbit is based on ranging data. Star trackers and gyros are used for satellite attitude determination. The attitudes of the imager and the satellite differ; that of the former is set by adjusting the satellite attitude using landmark analysis. Landmark analysis is performed swath by swath, and the bias of the attitudes between the satellite and the imager are determined using landmark analysis results for the whole observation area.

Band-to-band co-registration is determined by direct pattern matching between bands for each full-disk swath, and the displacement between bands is then related to temperatures of optical systems. Calculation of co-registration correction parameters is based on the regression between them.

## 3.2 Validation of registration

Attitude correction using landmarks was begun on 16 January 2015. Figure 3-1 shows image displacement of Himawari standard data. Before landmark attitude correction was started, there were large displacements in images, especially in the east-west direction. As shown in Figure 3-1 (left), east-west displacement was approximately 1,246 μrad (44.5 km at the sub-satellite point (SSP)), and north-south displacement was 16.24 μrad (1.8 km). As shown in Figure 3-1 (right), image displacement after the introduction of landmark attitude correction is small at around 10.6 μrad (0.38 km) in the east-west direction and 1.1 μrad (0.04 km) in the north-south direction.

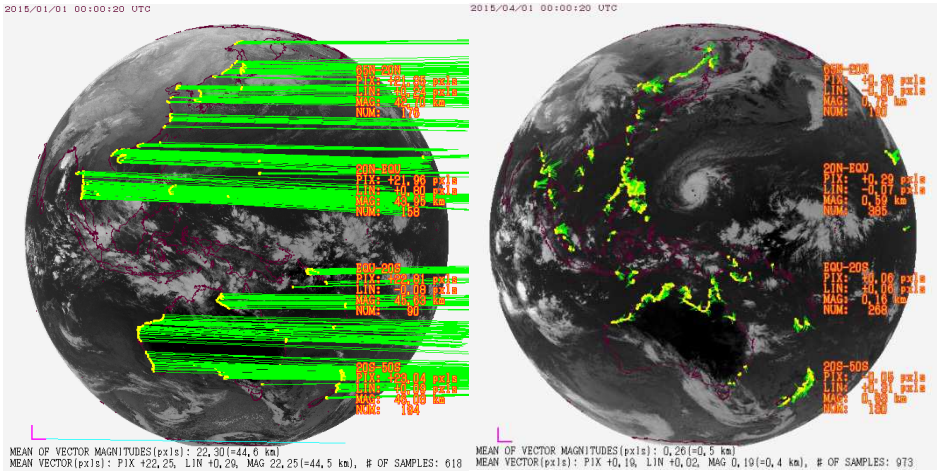


Figure 3-1 Displacement for band 7 before landmark correction on 1 January 2015 (left) and after landmark correction on 1 April 2015 (right). Yellow dots show reference points for computation of displacement. Segments connected with yellow dots represent the directions and magnitudes of displacement at each reference point. The short magenta segments at the bottom-left of Figure 3-1 and 3-2 represent the unit length of displacement magnitude, which is 28 μrad, or one pixel, for infrared bands.

### 3.3 Validation of band-to-band co-registration

Band-to-band co-registration correction was begun on 26 March 2015 in all bands. Figure 3-2 shows the co-registration of bands 1, 7, 8 and 15 compared to that of band 13. Displacement is less than 14 μrad (0.5 km). The co-registration results for other bands are similar except that for band 5, which is about 28 μrad (1 km).

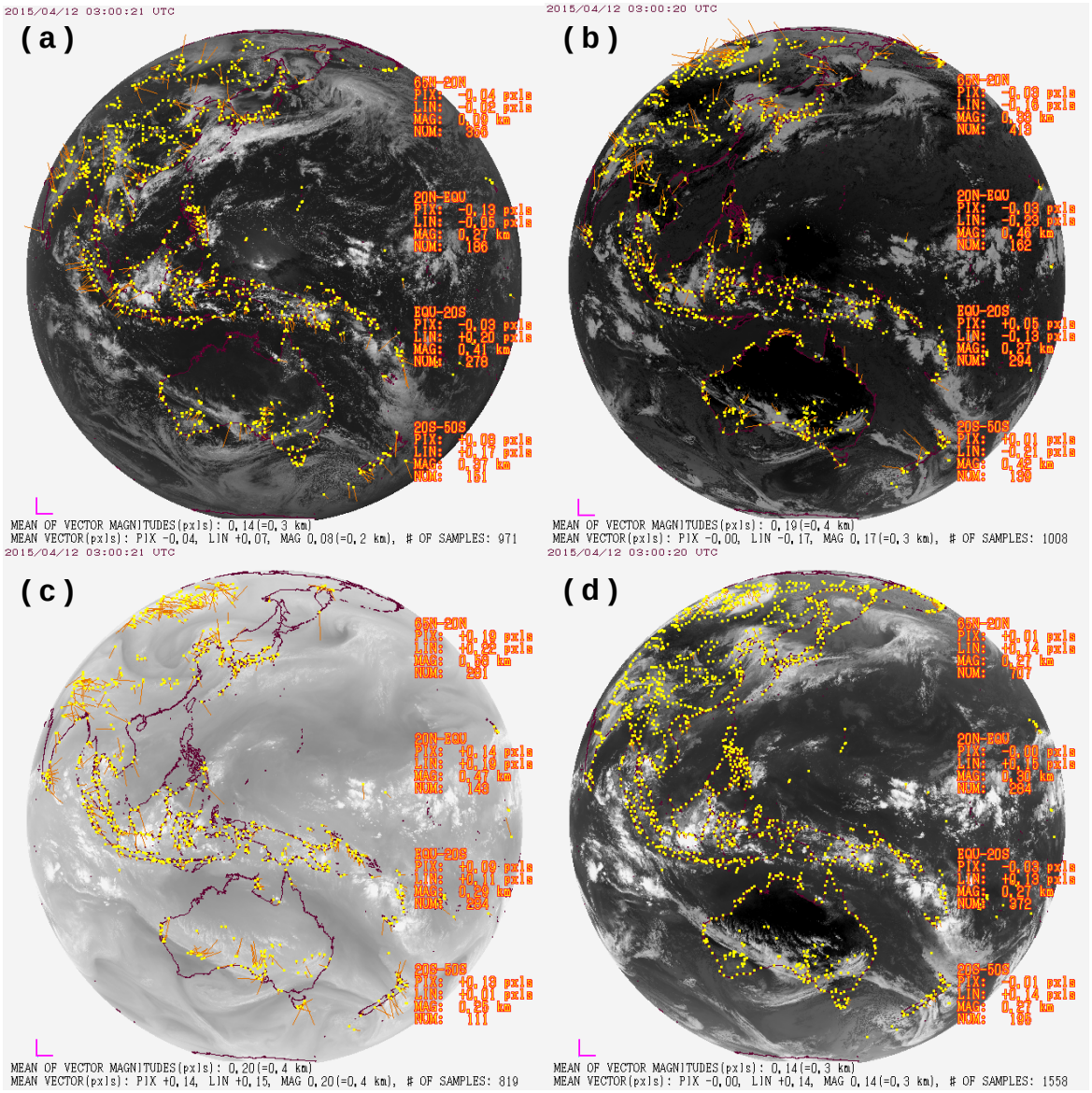


Figure 3-2 (a) co-registration of band 1 compared to that of band 13 at 03:00 UTC on 12 April 2015; (b) the same for band 7; (c) the same for band 8; and (d) the same for band 15. Dots and segments show reference points and their magnitudes as per Figure 3-1.

# 4 CALIBRATION

AHI has on-board calibration references: a blackbody for infrared bands and a solar diffuser for visible and near infrared bands. Inter-calibration and vicarious calibration approaches are planned to improve its reliability with reference to MTSAT observation, hyper-sounder observation (such as Metop-A/IASI, Metop-B/IASI, Aqua/AIRS and S-NPP/VIIRS types), lunar irradiance modeling and simulated radiance.

## 4.1 On-board calibration basics

For calibration of collected data, AHI has a blackbody as an ICT and a solar diffuser as a solar calibration target (SCT). Using these targets, linear and bias calibration coefficients are derived to allow conversion of raw data counts for detector samples into radiances.

The ICT is temperature-controlled with heaters and generates constant radiance. It is referred as a hot reference along with space view observations used as cold references for infrared bands. AHI observes the ICT every 10 minutes to enable the relation of radiance measured by the infrared bands to that of the hot reference. Deep space viewing is performed for every swath observation to give a measurement for the dark reference.

This is the first time an SCT has been installed on a JMA imager on board a geostationary meteorological satellite. It is made of Spectralon material manufactured by Labsphere. The MODerate resolution Imaging Spectroradiometer (MODIS) on board the Aqua/Terra satellites has the same equipment for on-board calibration. The SCT reflects and diffuses sunlight for observation by detectors. The SCT is used as a bright reference for visible and near-infrared bands together with the space view observations used as dark references. JMA plans to implement SCT observation twice a month. Current calibration coefficients for visible and near-infrared bands are based on ground testing. JMA plans to update the operational calibration parameters based on SCT observations by the start of AHI operation.

## 4.2 Post-launch calibration for infrared bands

### 4.2.1 Validation based on hyper-spectral sounder data

An infrared calibration approach developed under the Global Space-based Inter-Calibration System (GSICS) project involves the use of hyper-spectral infrared sounders (a.k.a. hyper sounders) such as the Infrared Atmospheric Sounding Interferometer (IASI) on board EUMETSAT's Metop satellite and the Atmospheric InfraRed Sounder (AIRS) on board NASA's Aqua satellite (Gunshor 2006; Tobin 2006; Tahara 2009). To compare observations made by an imager on board a geostationary (GEO) satellite with observation data from hyper sounders, this approach involves the generation of a super-channel cloning the broad channel of the imager on board the GEO satellite by minimizing the spectral response difference. This supports investigation of sensor bias and related seasonal or diurnal variations. Figure 4-1 shows the time dependency of brightness temperature bias between the AHI and hyper sounders. There is no significant diurnal variation, and the bias is less than 1 K for each band. The MSC website[2] includes a calibration monitoring page for the MTSAT series based on this approach. AHI results will also be provided on the same page.

[2] http://ds.data.jma.go.jp/mscweb/data/monitoring/calibration.html

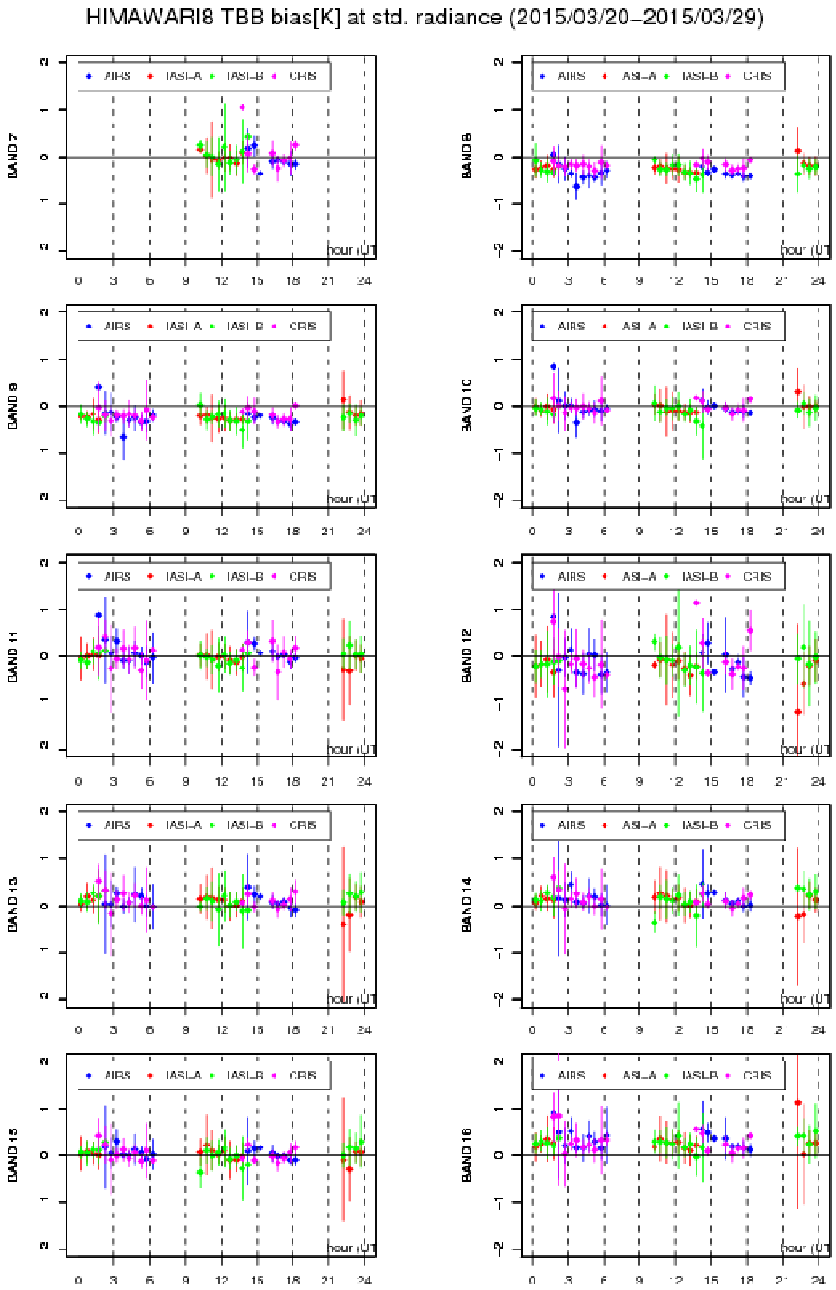


Figure 4-1 Diurnal variation of brightness temperature bias between the AHI and hyper sounders. Colors represent reference hyper sounders. Blue: Aqua/AIRS; red: Metop-A/IASI; green: Metop-B/IASI; magenta: S-NPP/CrIS. Only nighttime results are shown for band 7 (3.9 μm) to avoid the effects of sunlight.

### 4.2.2 Validation based on MTSAT-2 data

In addition to the GSICS approach outlined above, observation data from Himawari-8 are evaluated based on comparison with MTSAT-2 data. The comparison of information from two GEO imagers is useful in clarifying spatial and diurnal characteristics based on the advantages of the GEO satellite, i.e., wide coverage and frequent observation. Selection of the corresponding bands of MTSAT-2 for comparison with Himawari-8 data depends on images simulated using the RSTAR radiative transfer model (Murata et al. 2015). Differences in comparison involving GEO

images are caused by SRF and SSP discrepancies. Such image differences can be estimated using simulated images in which SRF and SSP are taken into account. Figure 4-2 compares Himawari-8/band 15 (12.4 μm) with MTSAT-2/IR2 (12.0 μm). The scatter plots show a discrepancy for significant irregularities such as large bias. The scatter plot distribution for actual observation (left panel) is consistent with that of simulation (right panel). This suggests that observation differences are attributable to discrepancies of SRF and SSP, and no significant anomaly is observed. The map and time-series representation of the differences (not shown) also show no significant anomalous characteristics.

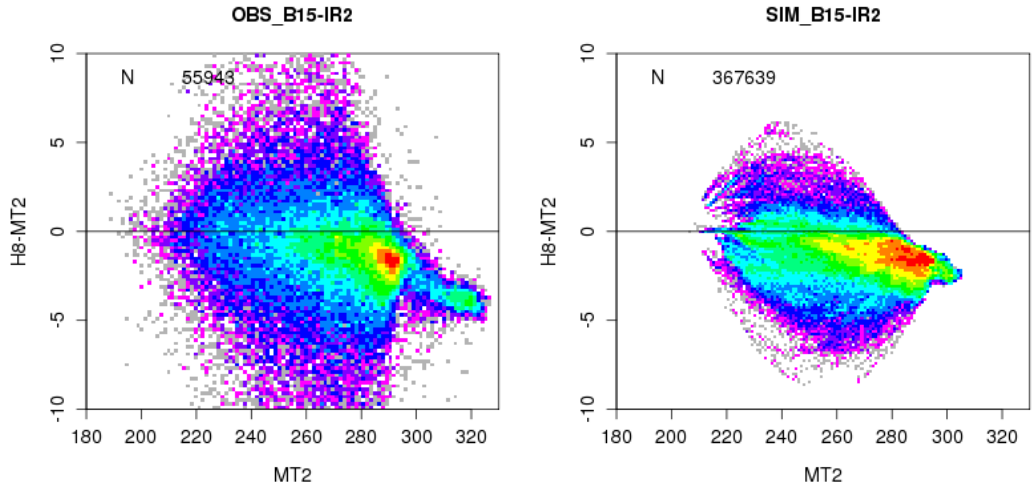


Figure 4-2 Results of comparison between Himawari-8/band 15 (12.4 μm) and MTSAT-2/IR2 (12.0 μm). The horizontal axis represents MTSAT-2 brightness temperature (TBB in K), and the vertical axis represents TBB difference between Himawari-8 and MTSAT-2. The panel on the left shows actual observation, while that on the right shows simulation.

## 4.3 Post-launch calibration for visible and near-infrared bands

A calibration method for visible bands is under investigation within the GSICS framework. JMA has also developed the following approaches for visible and near-infrared vicarious calibration:

A) Ray-matching with reference to S-NPP/VIIRS
B) Comparison with simulated radiance based on a radiative transfer model
C) Comparison with deep convective cloud measurement by MODIS
D) Comparison with the lunar irradiance model

In approach A), reference to radiance measured by S-NPP/VIIRS is made. VIIRS SRFs are similar to AHI SRFs, especially for near-infrared bands. Collocation datasets of VIIRS and AHI with similar geometric conditions and observation times are created, and both sets of measurements are compared. SRF differences are considered on the basis of radiative transfer computation results and information from the SBAF (spectral band adjustment factors) database developed by NASA, which is available on the web page[3].

[3] http://angler.larc.nasa.gov/cgi-bin/site/showdoc?mnemonic=SBAF

Approach B) was developed under collaborative research with the Atmosphere and Ocean Research Institute (AORI) at The University of Tokyo. The method involves reference to simulated radiance over pseudo-invariant targets such as cloud-free ocean, cloud-free bare soil areas, uniform liquid cloud top and deep convective cloud top.

Approach C) was developed under the GSICS framework, and involves reference to radiance measured by Aqua/MODIS for deep convective cloud top.

Approach D) is based on a lunar irradiance model developed by USGS (Kieffer and Stone, 2005). The model has been used by GSICS for the lunar calibration community. Lunar irradiance computed from AHI observation images is compared with the modelled irradiance. The approach is useful for identifying long-term trends.

Figure 4-3 shows validation of visible and near-infrared band calibration based on approach A). As current calibration parameters are based on ground testing, the validation results show a discrepancy of several percent between measured and expected radiance. This is consistent with the results obtained using approach B).

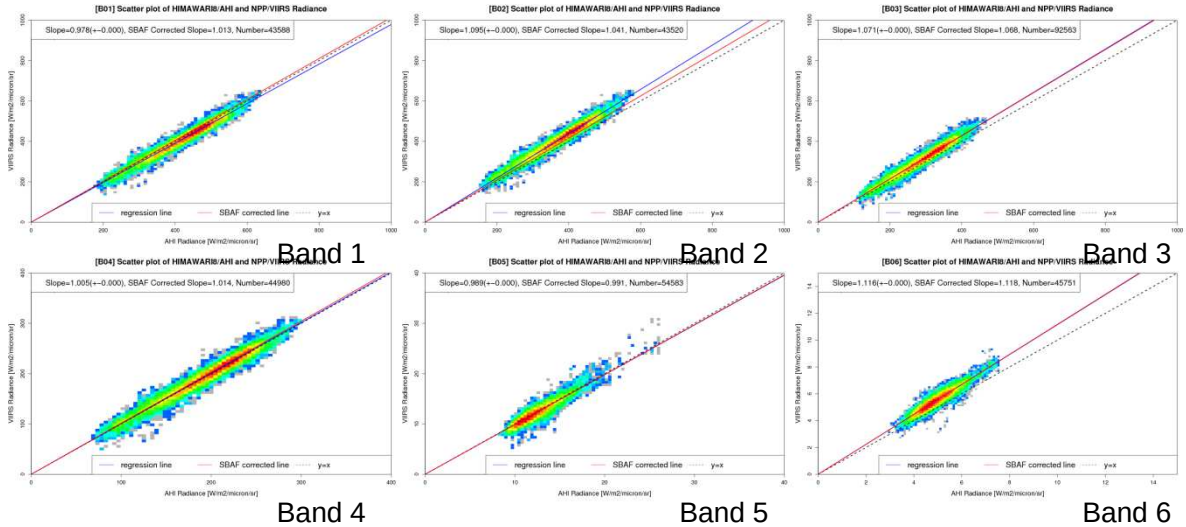


Band 1 Band 2 Band 3

Band 4 Band 5 Band 6

Figure 4-3 Validation of visible and near-infrared band calibration via the ray-matching approach. The horizontal and vertical axes represent radiance measured by the AHI and VIIRS, respectively. The solid blue and red lines show linear regression and correction based on the SBAF, respectively. The reference area is filtered based on spatial uniformity and brightness temperature measured via band 13. Relatively cold areas were selected for this validation.

# 5 PRODUCTS

## 5.1 Level 1

As outlined in Sections 1 and 2, the AHI's observation function is improved over that of the imager on board MTSAT-2 in terms of spatial resolution, observation frequency, the number of bands and other specifications. Figure 5-1 illustrates the spatial resolution improvement, which allows clearer identification of ground features such as rivers and landfills as well as the texture of clouds. The temporal resolution improvement also enables the production of striking images in typhoon analysis and other areas.

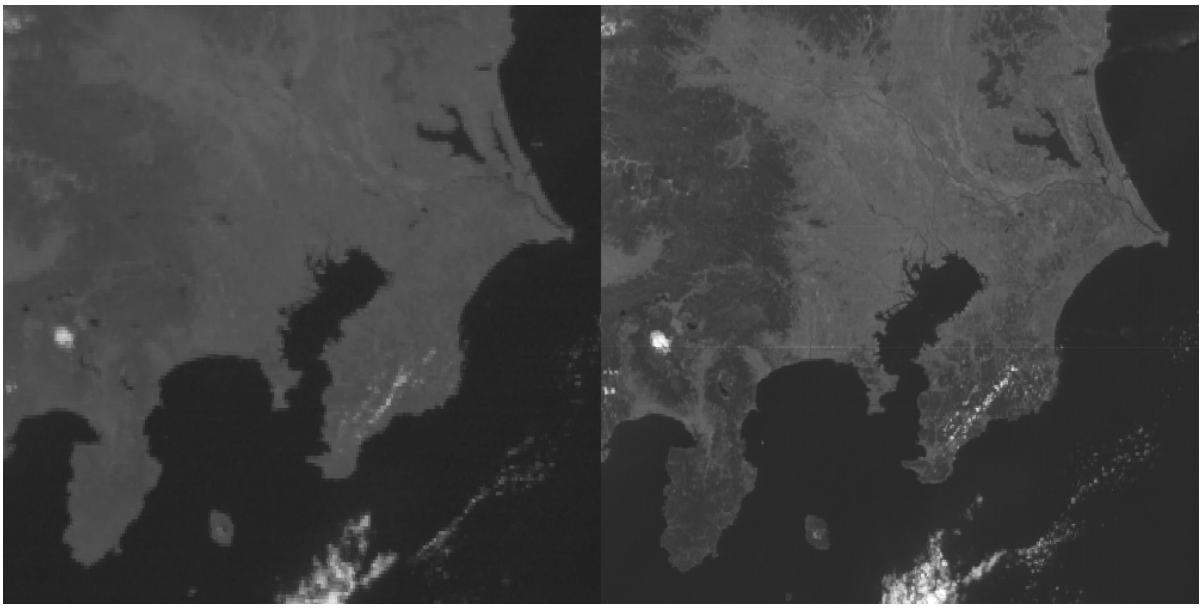

Figure 5-1 Image of Japan's Kanto region from the visible band of the MTSAT-2 imager (left) and the same from band 3 of the AHI (right) at 12:00 UTC on 31 March 2015. The spatial resolutions of these bands at SSP are 1.0 and 0.5 km for MTSAT-2 and AHI, respectively.

WMO provided the recipe of RGB composite images to facilitate the extraction of information on variables such as dust, vegetation and cloud droplet size (WMO, 2007). Figure 5-2 shows examples of RGB composites with a natural color image (left) and a dust image (right). The natural color image is a composite from bands 5 (1.6 μm), 4 (0.86 μm) and 3 (0.64 μm). Images from these three bands are assigned as red, green and blue components, respectively, which highlights ice and vegetation as light blue and green areas, respectively. The light-blue region over the ocean in Figure 5-2 (left) is drift ice, the white region over the ocean is liquid cloud, and the light-blue area over land appears to be snow. The dust image is a composite from bands 11 (8.6 μm), 13 (10.4 μm) and 15 (12.4 μm). The magenta area shows a volcanic plume, which can be distinguished from cloud as a gray area. The AHI's capability for such multi-band observation is beneficial for environmental monitoring and operational weather services.

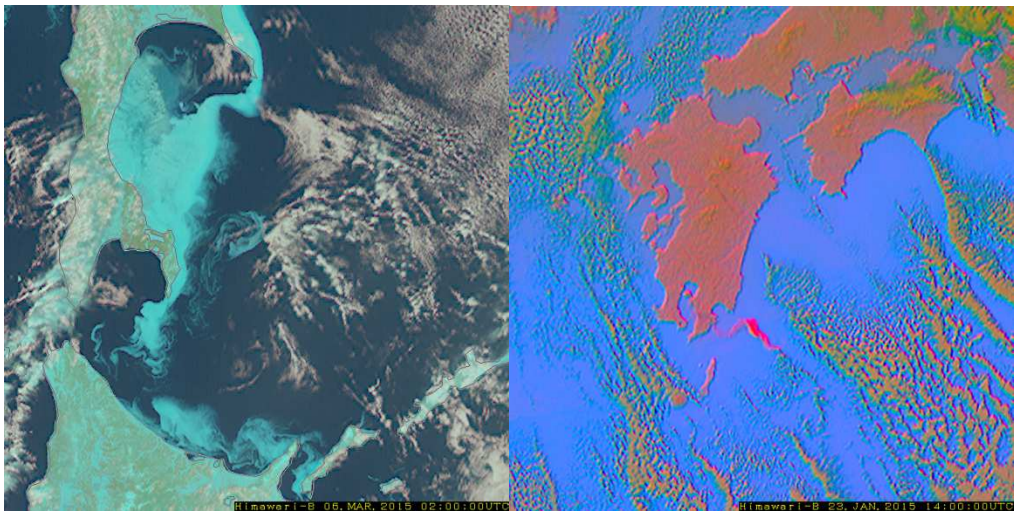

Figure 5-2 RGB composite images: natural color (left) and dust (right). The natural color image is a composite from bands 5 (1.6 μm), 4 (0.86 μm) and 3 (0.67 μm) representing red, green and blue, respectively, which highlights vegetation and ice. The image shows Japan's Hokkaido region at 02:00 UTC on 06 March 2015. The dust image is a composite from bands 11 (8.6 μm), 13 (10.4 μm) and 15 (12.4 μm). Its constitution is based on differences among these bands with volcanic ash highlighted in magenta. The image shows Japan's Kyushu region at 14:00 UTC on 23 January 2015.

## 5.2 Level 2

The Atmospheric Motion Vector (AMV) and Clear Sky Radiance (CSR) products derived from geostationary meteorological satellites play very important roles in Numerical Weather Prediction (NWP). JMA/MSC has developed Himawari-8 AMV and CSR products to be distributed via GTS when Himawari-8 becomes operational. The distribution of MTSAT-2 AMV and CSR via GTS will be terminated at the same time. JMA plans to distribute Himawari-8 AMV and CSR via JDDS (the JMA Data Dissemination System) from May to July 2015 so that NWP users can evaluate the products in advance. After Himawari-8 begins operation, MTSAT-2 AMV and CSR will continue to be provided via JDDS to support NWP users in transitioning smoothly from MTSAT-2 to Himawari-8. The status of the Himawari-8 AMV product will be reported by JMA-WP-04 at CGMS 43.

An objective cloud analysis information (OCAI) product to be made with data from Himawari-8 has been developed primarily for domestic users. It will also be provided to National Meteorological and Hydrological Services of Indonesia and Myanmar in response to requests.

A Himawari-8 aerosol optical depth (AOD) product has been developed. AOD data are retrieved from a lookup table as a function of reflectivity at visible and near-infrared bands (0.64 and 0.86 μm (ocean), 0.64 and 2.25 μm (land)). The aerosol type is assumed to be Asian dust, and the algorithm is not optimized for other types (e.g., haze). JMA will use Himawari-8 AOD to monitor Asian dust.

# 6 CONCLUSION

The next-generation geostationary meteorological satellite, Himawari-8, was successfully launched on 7 October 2014 and will start operation in July 2015. Himawari-8 features the new Advanced Himawari Imager, which has improved spatial resolution and observation frequency over those of its predecessor MTSAT-series

satellites. This working paper reports on the current status of AHI navigation and calibration. Validation results show that navigation error and co-registration error are less than one pixel, and no significant bias or diurnal variation in infrared bands is observed. As the current calibration parameters for the visible and near-infrared bands are based on ground testing, some of visible and near-infrared bands exhibit discrepancies of several percent between measured and expected radiance. JMA plans to update the calibration and navigation process by the time the AHI enters operation.

The imager's enhanced observation capability is expected to provide a greater wealth of information, including spatially finer images, temporally rich content such as animation of developing weather conditions, extensive RGB images and physical products. This is expected to contribute to advanced nowcasting services and short-range weather forecasting systems.

## 7 ACKNOWLEDGEMENT

JMA/MSC appreciates the input of all contributors to the validation of the AHI commissioning dataset, especially the NOAA/NESDIS ABI calibration team.

## 8 REFERENCES

Gunshor, M. M., T. J. Schmit, W. P. Menzel and D. C. Tobin, 2006, Intercalibration of the newest geostationary imagers via high spectral resolution AIRS data. Conference on Satellite Meteorology and Oceanography, 14th, Atlanta, GA, 29 January – 2 February 2006 (preprint). Boston, MA, American Meteorological Society, 2006, Paper P 6.13.

Kieffer, Hugh H. and Thomas C. Stone, 2005, The spectral irradiance of the moon, The Astronomical Journal, 129: 2887 – 2901

Murata, H., M. Takahashi and Y. Kosaka, 2015, VIS and IR bands of Himawari-8/AHI compatible with those of MTSAT-2/Imager, Meteorological Satellite Center Technical Note, No. 60, 1-18

Tobin, D.C., H. E. Revercomb, C. C. Moeller and T. Pagano, 2006, Use of Atmospheric Infrared Sounder high-spectral resolution spectra to assess the calibration of Moderate Resolution Imaging Spectroradiometer on EOS Aqua. J. Geophys. Res., 111, D09S05, DOI: 10.1029/2005JD006095

Tahara, Y. and K. Kato, 2009, New Spectral Compensation Method for Inter-calibration Using High Spectral Resolution Sounder, Meteorological Satellite Center Technical Note, No. 52, 1-37

WMO, 2007, Final report of RGB Composite Satellite Imagery Workshop, Boulder USA, http://www.wmo.int/pages/prog/sat/documents/RGB-1_Final-Report.pdf

## Appendix Summary of operational system IOT results

| Band | EW direction [urad] | | | NS direction [urad] | | |
|---|---|---|---|---|---|---|
| | IOT measurement | Specification | Ground test result | IOT measurement | Specification | Ground test result |
| 1 | 12 | ≦ 28 | 19 | 12 | ≦ 28 | 10 |
| 2 | 14 | ≦ 28 | 21 | 12 | ≦ 28 | 10 |
| 3 | 9 | ≦ 14 | 11 | 9 | ≦ 14 | 7 |
| 4 | 16 | ≦ 28 | 21 | 13 | ≦ 28 | 11 |
| 5 | 28 | ≦ 56 | 37 | 20 | ≦ 56 | 18 |
| 6 | 34 | ≦ 56 | 40 | 23 | ≦ 56 | 18 |
| 7 | 45 | ≦ 56 | 41 | 32 | ≦ 56 | 21 |
| 8 | - | ≦ 56 | 42 | - | ≦ 56 | 25 |
| 9 | - | ≦ 56 | 42 | - | ≦ 56 | 26 |
| 10 | - | ≦ 56 | 44 | - | ≦ 56 | 26 |
| 11 | 49 | ≦ 56 | 44 | 45 | ≦ 56 | 28 |
| 12 | 50 | ≦ 56 | 44 | 45 | ≦ 56 | 30 |
| 13 | 41 | ≦ 56 | 45 | 44 | ≦ 56 | 30 |
| 14 | 43 | ≦ 56 | 47 | 41 | ≦ 56 | 31 |
| 15 | 45 | ≦ 56 | 46 | 41 | ≦ 56 | 32 |
| 16 | - | ≦ 56 | 48 | - | ≦ 56 | 34 |

Table A-1 IFOV size for the EW and NS directions. IFOV size is defined from the spatial response function as an angle whose width is 50% of the total integrated spatial response function. As the validation here is examined using coastline images, absorption bands are not applicable to this approach.

| Band | Sampling distance [urad] | Specification [urad] |
|---|---|---|
| 1 | 27.9 | ≦ 28 |
| 2 | 27.9 | ≦ 28 |
| 3 | 14.0 | ≦ 14 |
| 4 | 27.9 | ≦ 28 |
| 5 | 55.7 | ≦ 56 |
| 6 | 55.7 | ≦ 56 |
| 7 | 55.7 | ≦ 56 |
| 8 | 55.7 | ≦ 56 |
| 9 | 55.7 | ≦ 56 |
| 10 | 55.7 | ≦ 56 |
| 11 | 55.7 | ≦ 56 |
| 12 | 55.7 | ≦ 56 |
| 13 | 55.8 | ≦ 56 |
| 14 | 55.8 | ≦ 56 |
| 15 | 55.5 | ≦ 56 |
| 16 | 55.5 | ≦ 56 |

Table A-2 Angular sampling distance for the EW direction. Distance is computed from a number of EW-direction samples and mirror angle information.

| Band | SNR |
|---|---|
| 1 | 793.2 |
| 2 | 763.7 |
| 3 | 524.3 |
| 4 | 454.4 |
| 5 | 1046.5 |
| 6 | 804.4 |
| 7 | 201.7 / 366.7* |
| 8 | 249.5 |

| Band | SNR |
|---|---|
| 9 | 1619.1 |
| 10 | 460.8 |
| 11 | 1891.7 |
| 12 | 1631.2 |
| 13 | 1183.2 |
| 14 | 1649.6 |
| 15 | 1318.3 |
| 16 | 463.8 |

* SNRs without/with the noise reduction process are shown.

Table A-3 Signal-to-noise ratio (SNR) for visible and near-infrared bands (left) and infrared bands (right). SNR estimation is based on blackbody observation for infrared bands and on solar diffuser observation for visible and near-infrared bands. JMA plans to introduce a noise reduction process into ground processing software for band 7. SNRs for band 7 with and without noise reduction are shown.

| Band | Spec. | Output level | "100% albedo" [W/m^2/sr/um] |
|---|---|---|---|
| 1 | ≧ 1.1 | 1.2 | 641.5092 |
| 2 | ≧ 1.2 | 1.2 | 601.9766 |
| 3 | ≧ 1.2 | 1.4 | 519.3457 |
| 4 | ≧ 1.05 | 1.4 | 309.3583 |
| 5 | ≧ 1.0 | 1.1 | 77.1412 |
| 6 | ≧ 1.0 | 1.2 | 23.9163 |

| Band | Higher Tb. | | | Lower Tb. | |
|---|---|---|---|---|---|
| | Target temp. | Spec. | Output level | Spec. | Output level |
| 7 | 400K | ≦ 1 | 0.91 | ≧ 0 | 0.09 |
| 8 | 270K | ≦ 1 | 0.42 | ≧ 0 | 0.18 |
| 9 | 300K | ≦ 1 | 0.62 | ≧ 0 | 0.18 |
| 10 | 285K | ≦ 1 | 0.51 | ≧ 0 | 0.18 |
| 11 | 330K | ≦ 1 | 0.80 | ≧ 0 | 0.17 |
| 12 | 300K | ≦ 1 | 0.68 | ≧ 0 | 0.21 |
| 13 | 330K | ≦ 1 | 0.72 | ≧ 0 | 0.15 |
| 14 | 330K | ≦ 1 | 0.81 | ≧ 0 | 0.18 |
| 15 | 330K | ≦ 1 | 0.61 | ≧ 0 | 0.16 |
| 16 | 300K | ≦ 1 | 0.49 | ≧ 0 | 0.16 |

Table A-4 Dynamic ranges for visible and near-infrared bands (left) and infrared bands (right).
For visible and near-infrared bands, the output saturation level meets the specifications. A value of 1.0 represents a 100% albedo as shown in the table on the left. For infrared bands, the deep space count and the output level for a blackbody with a specific temperature meets the specifications. 1.0 represents the saturation level for each band.